On the constitutive relations for catalyst coated membrane applied to in-situ fuel cell modeling

CrossMark

Ramin M.H. Khorasany, Marc-Antoni Goulet, Alireza Sadeghi Alavijeh, Erik Kjeang*, G. Gary Wang, R.K.N.D. Rajapakse

School of Mechatronic Systems Engineering, Simon Fraser University, 250-13450 102 Avenue, Surrey, BC V3T 0A3, Canada

HIGHLIGHTS

- An elastic–viscoplastic constitutive relation is developed for CCMs.
- Membrane based mechanical models may overestimate stresses during cyclic operation.
- The CCM model predicts higher plastic strain during hygrothermal loading.
- Treatment of the CCM as a composite object is recommended for in-situ simulations.

ARTICLE INFO

ABSTRACT

The elastic–viscoplastic behavior of catalyst coated membranes (CCMs) used in polymer electrolyte membrane fuel cells is investigated in this work. Experimental results reveal significant differences between the mechanical properties of a pure perfluorosulfonic acid ionomer membrane and the corresponding CCM under uniaxial tension and cyclic loading. An elastic–viscoplastic constitutive model that is capable of capturing the time dependent response of the CCM at different humidity and temperature conditions is developed and validated against ex-situ experimental results. The validated model is then utilized to simulate the in-situ mechanical response of the CCM when treated as a composite object bonded through the ionomer phase. When compared to a conventional membrane model, the CCM model predicts considerably lower maximum stress and higher plastic strain under typical fuel cell operating conditions and improved plastic strain recovery during hygrothermal unloading. These results reflect the weaker nature of the CCM material which yields at a lower stress than the membrane and may lead to elevated plastic deformation when exposed to hygrothermal cycles in a constrained fuel cell environment. Hence, coupled CCM implementation is generally recommended for finite element modeling of fuel cells.

1. Introduction

The polymer electrolyte membrane fuel cell (PEMFC) is a promising clean technology for converting chemical energy into electrical energy for automotive, stationary, and portable applications. The potential environmental benefits of these technologies are immense. Depending on the source of the hydrogen, greenhouse gas emissions can be reduced significantly as compared to internal combustion engines. Modern PEMFCs use a perfluorosulfonic acid (PFSA) membrane such as Nafion to separate the reactant gases while maintaining ionic conductivity between anode and cathode. The membrane is normally coated with a catalyst layer on each side to form a catalyst coated membrane (CCM), which is the reactive core of the membrane electrode assembly (MEA) of a fuel cell. When situated inside an MEA, membrane stability is challenged by chemical and mechanical stressors during fuel cell operation. The transition between low and high power consumption in a typical operating cycle of a PEMFC generates cyclic hygrothermal stresses in the membrane that result in mechanical degradation. It has been proposed that these cyclic stresses may lead to the creation of small holes in the areas that are under high stress concentration [1]. This ultimately results in MEA failure through hydrogen leaks, which is a serious safety hazard. Insufficient membrane durability is one of the main constraints in the commercialization of PEMFCs for automotive applications [2].

In an ongoing effort to understand the mechanical characteristics of commonly employed PFSA membranes, researchers have conducted tensile experiments on membrane samples at different humidity and temperature conditions. Tang et al. [3] were amongst the first researchers who conducted experiments to measure the Young's modulus, yield stress, breaking stress and breaking strain of a PFSA membrane under controlled ambient conditions. They concluded that as the temperature or humidity increases, the Young's modulus and yield stress decrease. They also found that temperature changes have a more substantial effect on the breaking strain and stress values compared to humidity changes. In a more recent work, Tang et al. [4] conducted experiments to examine the mechanics of a class of reinforced PFSA membranes. They determined that a reinforced membrane has a much higher Young's modulus compared to unreinforced membranes. Kusoglu et al. [5] conducted experiments to study the mechanical behavior of a swelled membrane in liquid water, and found that the transition between the linear and nonlinear parts of the stress—strain curves was not possible to discern. While many studies have investigated the mechanical properties of PFSA membranes, there is still limited understanding of the fracture behavior of membranes. In their work, Aindow and O'Neill [6] investigated the fatigue fracture response of the membrane under the application of cyclic uniaxial stresses. It was discovered that membrane stability can be increased exponentially by reducing the level of mechanical stress.

While ex-situ membrane properties are relatively straightforward to measure, its mechanical behavior in-situ during fuel cell operation is difficult to determine experimentally. Consequently, numerical models can provide valuable insight. However, numerical in-situ modeling of a membrane in an MEA carries significant challenges as well, such as translation of tensile properties into an environment based on internal expansion and contraction in a fixed reference frame and dynamic changes in membrane liquid water uptake. Several recent contributions have addressed these challenges in order to predict the stresses and strains created in the membrane during hygrothermal operating cycles [7—13].

One of the preliminary constitutive relations used to model the in-situ mechanical response of the membrane assumed a linear response for the stresses below the yield point and a plastic response after that. Kusoglu et al. [14] initially assumed a linear elastic, perfectly plastic constitutive behavior for the membrane, which was later modified [15] by adopting linear-elasticity with isotropic-hardening plasticity to study the in-situ response of the membrane. However, the assumption of a linear elastic response from the membrane is not very accurate as the published experimental results reveal that, similar to many other polymers, the membrane modulus depends on the strain rate [12].

One of the main mechanical characteristics of polymers in general, and the membrane in particular, is the time dependent behavior. This time dependent response of the material can be observed through creep and stress relaxation measurements such as those performed by Solasi et al. [16]. They noted that the creep mechanism is consistent across a wide range of hydration levels. It was also discovered that membrane samples at the breaking point do not experience necking. In another work, Solasi's group [17] proposed a two-layer viscoplastic model.

Silberstein and Boyce [18] were amongst the first researchers in the field who addressed both the loading and unloading part of the membrane mechanical behavior with numerical modeling. They developed an elastic—viscoplastic constitutive relation capable of capturing the true response of the membrane under both mechanical and hygrothermal loadings. Later on, Silberstein et al. used the elastic—viscoplastic model to study the effect of biaxial tensioning on the membrane [19] and to investigate the response of Nafion/GDL (Gas Diffusion Layer) under constrained swelling [20].

The constitutive relations developed by Silberstein and Boyce were recently used by other groups for simulation purposes [21,22].

All previous modeling studies in this field have considered the membrane as a separate object when situated in an MEA. However, within and operating PEMFC, the catalyst layers are typically bonded to the membrane via the ionomer phase in the catalyst layer, constituting a catalyst coated membrane (CCM). A previous experimental study by our group [23] revealed that CCMs exhibit significantly different mechanical behavior than pure PFSA membranes, and would therefore respond differently under externally applied loads. Hence, the first objective of the present work is to develop a fundamental constitutive model for a standard CCM that can be utilized to simulate the mechanical response of the CCM as a composite object. The model is intended to capture the response of the CCM in uniaxial loading and to predict the relation between the stress and strain during the unloading. The second objective of this work is to apply the obtained model to study the in-situ response of the CCM under hygrothermal cyclic loading inside a fuel cell.

2. Theory

The experimental results presented in our previous study [23] suggest that although the CCM differs from the pure membrane, it still possesses many of the same fundamental properties of the polymer membrane. In other words, the stress—strain behavior of the CCM has the following characteristics: time-dependency, rate-dependency, humidity-dependency, and temperature-dependency. In addition, it was determined that the membrane is the main load bearing component of the CCM and that the catalyst layers act as a reinforcement [23]. Therefore, it may be assumed that the constitutive relation for the CCM has a form similar to that of the membrane. The membrane has a molecular network which is made of interconnected molecular chains. The stress in the membrane is the summation of the stress caused by the network resistance and intermolecular resistance. The intermolecular mechanism resists membrane elongation for relatively low strains. At higher strain levels, it is the network mechanism that resists the membrane elongation. On the other hand for low levels of elongations, it is the intermolecular mechanism that contributes to the stress and for relatively high levels of strain the network mechanism has a more substantial effect in the stress contribution. The intermolecular mechanism (mechanism A, Fig. 1a) is assumed to be a linear elastic spring in series with a viscoplastic dashpot [18]. The network mechanism (mechanism B, Fig. 1a) is assumed to be a nonlinear spring in parallel with the intermolecular mechanism.

Under typical automotive fuel cell operating conditions, the electronic loads often fluctuate significantly, which gives rise to unsteady hygrothermal conditions with respect to the CCM. Indeed, this will cause fluctuating stress and strain distributions in the cell. In order for a constitutive model to simulate the real stress and strain distribution in the CCM, the model must be able to capture the mechanical behavior not only under the loading condition but
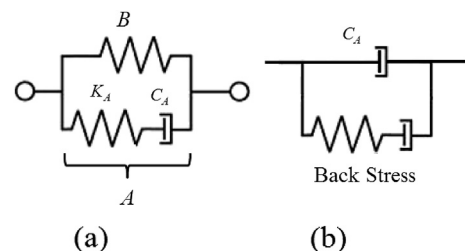

Fig. 1. Rheological representation of (a) the constitutive model for the CCM and (b) the back stress mechanism.

also under the unloading condition. Numerical investigations have revealed that the model in Fig. 1a predicts a linear unloading response, while the unloading characteristics of the CCM are dominated by nonlinear terms [24]. More information regarding this type of models for polymers can be found in Refs. [24–26]. Therefore, the basic model described in Fig. 1a is incapable of capturing the cyclic response of the CCM and should be modified accordingly. When the plastic deformation state is reached, a back stress component is locally developed that during the unloading eases the reverse deformation. As illustrated in Fig. 1b, the back stress mechanism is positioned in parallel with the viscoplastic dashpot of the intermolecular mechanism (mechanism A).

The network and intermolecular mechanisms in Fig. 1 are assumed to be in parallel. Therefore, in tensorial form we can write

$$\mathbf{F}_A = \mathbf{F}_B = \mathbf{F} \tag{1}$$

where $\mathbf{F}_A$ and $\mathbf{F}_B$ are the deformation gradients of the intermolecular and network mechanisms, respectively. Since these two mechanisms are in parallel, the total Cauchy stress ($\mathbf{T}$) is the sum of the contributions from the intermolecular ($\mathbf{T}_A$) mechanism and the network mechanism ($\mathbf{T}_B$)

$$\mathbf{T} = \mathbf{T}_A + \mathbf{T}_B \tag{2}$$

Based on the experimental results reported in Ref. [23], the CCM may experience significant plastic deformation during typical operating conditions. Therefore, the contribution of the plastic deformation in the total stress should be separated from that of the elastic deformation. The principles of continuum mechanics are applied to separate the elastic portion of the deformation gradient from the plastic portion by

$$\mathbf{F} = \mathbf{F}_A^e \mathbf{F}_A^p \tag{3}$$

where $\mathbf{F}_A^e$ and $\mathbf{F}_A^p$ are the elastic and plastic portions of the deformation gradient from the intermolecular mechanism, respectively. The velocity gradient ($\mathbf{L}$), is defined to be

$$\mathbf{L} = \dot{\mathbf{F}}\mathbf{F}^{-1} \tag{4}$$

where the dot indicates the time derivative. The velocity gradient can be decomposed into the rate of spin and stretching denoted by $\mathbf{W}$ and $\mathbf{D}$, respectively, as

$$\mathbf{L} = \mathbf{D} + \mathbf{W} \tag{5}$$

Therefore, for the plastic part of deformation of the intermolecular mechanism, we can write

$$\mathbf{L}_A^p = \mathbf{D}_A^p + \mathbf{W}_A^p \tag{6}$$

where

$$\mathbf{L}_A^p = \dot{\mathbf{F}}_A^p (\mathbf{F}_A^p)^{-1} \tag{7}$$

Without loss of generality, we can assume that the spin is negligible $\left(\mathbf{W}_A^p \approx 0\right)$ [25], and therefore from Eqs. (6) and (7), we have

$$\mathbf{D}_A^p = \dot{\mathbf{F}}_A^p (\mathbf{F}_A^p)^{-1} \tag{8}$$

It is well known that for a wide range of materials, the plastic flow is initiated and propagated by the shear stresses according to [24]

$$\mathbf{D}_A^p = \dot{\gamma}_A^P \frac{\mathbf{T}'_{A-BS}}{\sqrt{2}\tau_{A-BS}} \tag{9}$$

$$\mathbf{T}_{A-BS} = \mathbf{T}_A - \mathbf{T}_{BS} \tag{10}$$

$$\dot{\gamma}_A^P = \dot{\gamma}^0 \exp\left[\frac{-\Delta G}{k_b \theta}\right] \sinh\left[\frac{\Delta G}{k_b \theta} \frac{\tau_{A-BS}}{s_A}\right] \tag{11}$$

$$\mathbf{T}_{A-BS} = \mathbf{T}_{A-BS} - (1/3)(\mathbf{T}_{A-BS1} + \mathbf{T}_{A-BS2} + \mathbf{T}_{A-BS3}) \tag{12}$$

$$\tau_{A-BS} = \sqrt{(1/2)\left(\left(\mathbf{T}'_{A\_BS1}\right)^2 + \left(\mathbf{T}'_{A\_BS2}\right)^2 + \left(\mathbf{T}'_{A\_BS3}\right)^2\right)} \tag{13}$$

where $\dot{\gamma}_A^P$ governs the magnitude of the inelastic velocity gradient, θ is the absolute temperature, ΔG is the activation energy, k_b is the Boltzmann's constant, s_A is the shear resistance for the intermolecular mechanism, $\mathbf{T}_{BS}$ is the Cauchy stress contribution of the back stress component, $\mathbf{T}_{A-BS1}$, $\mathbf{T}_{A-BS2}$ and $\mathbf{T}_{A-BS3}$ are the principle stresses of stress tensor $\mathbf{T}_{A-BS}$, and $\mathbf{T}'_{A\_BS1}$, $\mathbf{T}'_{A\_BS2}$ and $\mathbf{T}'_{A\_BS3}$ are the principal stresses of the deviatoric part of the Cauchy stress tensor $\mathbf{T}_{A-BS}$. The shear resistance for the intermolecular mechanism is assumed to be

$$s_A = s_{A1} + s_{A2} - s_{A3} \tag{14}$$

$$\dot{s}_{A1} = h_{A1}(1 - s_{A1}/s_{A1-sat})\dot{\gamma}_A^P \tag{15}$$

$$s_{A2} = h_{A2}\left(\sqrt{\left(\lambda_{1A}^2 + \lambda_{2A}^2 + \lambda_{3A}^2\right)/3} - 1\right) \tag{16}$$

$$\dot{s}_{A3} = h_{A3}(1 - s_{A3}/s_{A3-sat})\dot{\gamma}_A^P \tag{17}$$

where s_{A1}, s_{A1-sat}, s_{A3}, s_{A3-sat}, h_{A1}, h_{A2} and h_{A3} are material constants that should be determined. λ_{1A}, λ_{2A} and λ_{3A} are the principal values of the gradient deformation tensor, $\mathbf{F}_A$. The Cauchy stress of the intermolecular mechanism can be derived as

$$\mathbf{T}_A = \frac{1}{J_A}\left(\mathbf{F}_A^e \mathbf{S}_A \mathbf{F}_A^{e^T}\right) \tag{18}$$

$$\mathbf{S}_A = 2\mu_A \mathbf{E}' + \kappa_A(tr\mathbf{E})\mathbf{I} \tag{19}$$

$$\mathbf{E} = \frac{1}{2}\left(\mathbf{F}_A^{e^T}\mathbf{F}_A^e - \mathbf{I}\right) \tag{20}$$

where $J_A = \det(\mathbf{F}_A^e)$, μ_A is the shear modulus, κ_A is the bulk modulus, and $\mathbf{I}$ is the second order identity tensor.

As can be seen from Fig. 1b, it is assumed that the deformation gradient of the back stress component is identical to the plastic portion of the deformation gradient of the intermolecular mechanism. Therefore,

$$\mathbf{F}_{BS} = \mathbf{F}_A^p \tag{21}$$

The velocity gradient of the back stress component can be derived as

$$\mathbf{D}_{BS}^p = \dot{\gamma}_{BS}^P \frac{\mathbf{T}'_{BS}}{\sqrt{2}\tau_{BS}} \tag{22}$$

$$\mathbf{T}_{BS} = \frac{2\mu_{BS}}{J_{BS}}\left(\mathbf{F}_{BS}^{e}\mathbf{E}_{BS}'\mathbf{F}_{BS}^{e^{T}}\right) \tag{23}$$

$$\mathbf{E}_{BS} = \frac{1}{2}\left(\mathbf{F}_{BS}^{e^{T}}\mathbf{F}_{BS}^{e} - \mathbf{I}\right) \tag{24}$$

$$\dot{\gamma}_{BS}^{P} = \dot{\gamma}^{0}\exp\left[\frac{-\Delta G}{k_{b}\theta}\right]\sinh\left[\frac{\Delta G}{k_{b}\theta}\frac{\tau_{BS}}{s_{BS}}\right] \tag{25}$$

$$\tau_{BS} = \sqrt{(1/2)\left(\left(T'_{BS1}\right)^{2} + \left(T'_{BS2}\right)^{2} + \left(T'_{BS3}\right)^{2}\right)} \tag{26}$$

$$\dot{s}_{BS} = h_{BS}(1 - s_{BS}/s_{BS-sat})\dot{\gamma}_{BS}^{P} \tag{27}$$

where μ_{BS} is the back stress shear modulus and $J_{BS} = \det(\mathbf{F}_{BS}^{e})$, T'_{BS1}, T'_{BS2} and T'_{BS3} are the principal stresses of the deviatoric part of the stress tensor, $\mathbf{T}_{BS}$.

The contribution of network resistance in the total stress can be calculated as

$$\mathbf{T}_{B} = \frac{1}{J_{B}}\mu_{B}\mathbf{B}_{B}' \tag{28}$$

$$\mathbf{B}_{B} = \mathbf{F}_{B}\mathbf{F}_{B}^{T} \tag{29}$$

where μ_{B} is the rubbery shear modulus, $\mathbf{B}_{B}$ is the left Cauchy–Green tensor and $J_{B} = \det(\mathbf{F}_{B})$.

The variations in temperature and humidity change both the kinematics of the deformation and the magnitude of the intermolecular and network resistances. Based on the kinematic changes,

the gradient deformation of the intermolecular resistance can be written as

$$\mathbf{F} = \mathbf{F}_{A}^{e}\mathbf{F}_{A}^{p}\mathbf{F}^{SE} \tag{30}$$

where $\mathbf{F}^{SE}$ is the deformation gradient due to hydration and thermal expansion. In terms of the changes in temperature, $\Delta\theta$, and relative humidity, ΔRH, $\mathbf{F}^{SE}$ can be written as

$$\mathbf{F}^{SE} = \lambda^{T-RH}\mathbf{I} = \left(1 + \alpha^{T}\Delta\theta + \alpha^{RH}\Delta RH\right)\mathbf{I} \tag{31}$$

where α^{T} is the thermal expansion coefficient and α^{RH} is the hydration expansion coefficient due to the change in relative humidity. For PFSA membranes, the values for α^{T} and α^{RH} are based on those reported in Ref. [15]. It is assumed that the hydration and thermal expansion of the membrane is isotropic and uniform. For the CCM, these properties were measured by our group using a dynamic mechanical analyzer. The hygrothermal expansion coefficients of the CCM and PFSA membrane used in this article are listed in Table 1.

The temperature and relative humidity variations also affect the kinematics of the network resistance mechanism as

Table 1
Hygrothermal expansion coefficients of the PFSA membrane and the CCM.

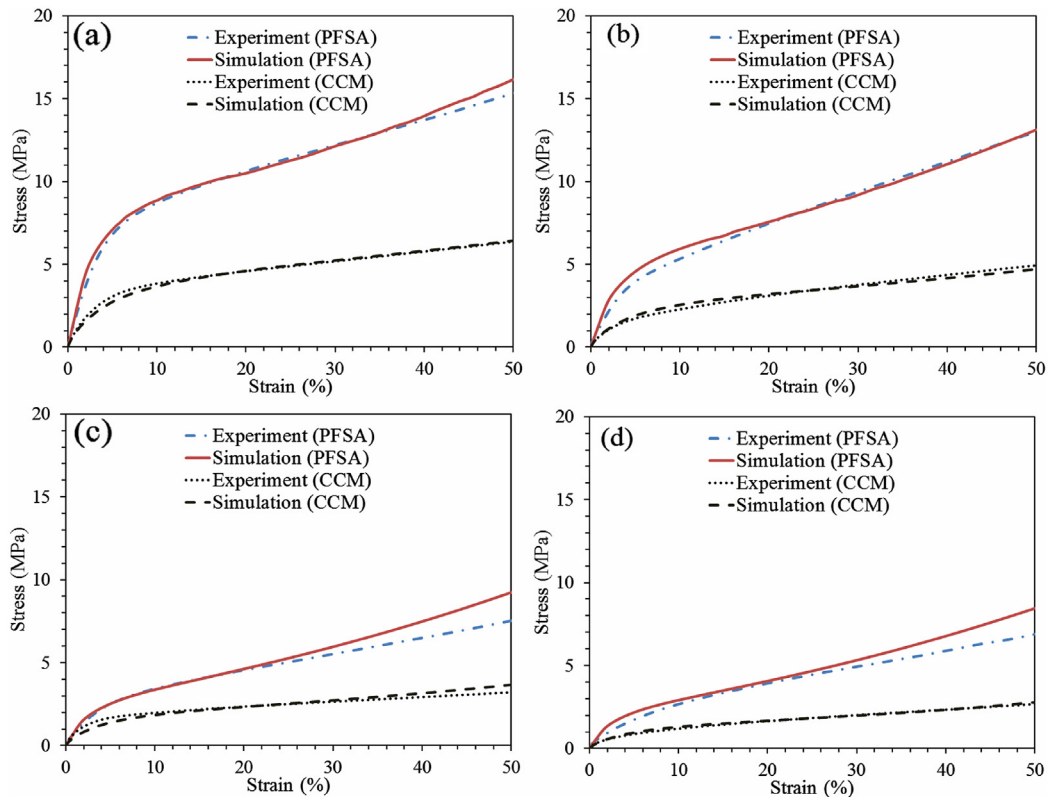|	α^{T} (K^{-1})	α^{RH} (%$^{-1}$)
PFSA	1.23×10^{-4}	1.33×10^{-3}
CCM	7.21×10^{-4}	4.84×10^{-4}

Fig. 2. Comparison between simulated and experimental results for the PFSA membrane and the CCM under uniaxial tensile stress at (a) 23 °C − 50% RH, (b) 23 °C − 90% RH, (c) 70 °C − 50% RH and (d) 70 °C − 90% RH.
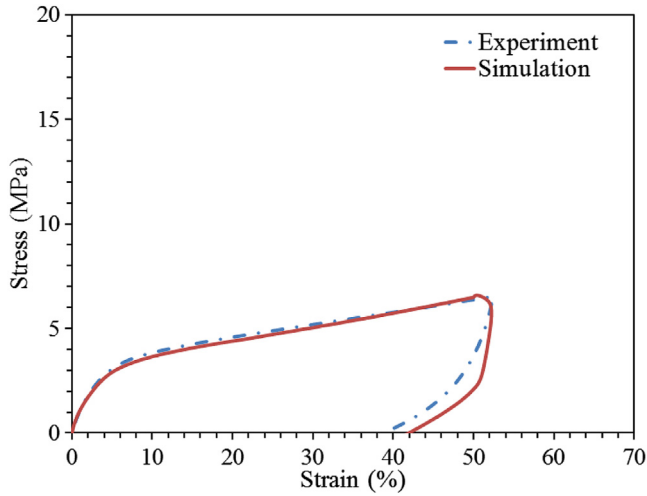
Fig. 3. Comparison between simulated and experimental results for the CCM under uniaxial loading and unloading at 23 °C and 50% RH.

$$\mathbf{F}_B = \mathbf{F}_B^m \mathbf{F}^{SE} \tag{32}$$

and the left Cauchy−Green tensor is modified to

$$\mathbf{B}_B^m = \mathbf{F}_B^m (\mathbf{F}_B^m)^T \tag{33}$$

The hygrothermal expansion also reduces the resistance in the network mechanism, and the total stress induced by the network mechanism can be written as

$$\mathbf{T}_B = \frac{1}{\lambda^{T-RH} J_B} \mu_B \mathbf{B}_B' \tag{34}$$

It should be emphasized that for both PFSA membrane and CCM, several key parameters are a function of hygrothermal conditions, including μ_A, s_{A1}, s_{A3}, μ_{BS} and s_{BS}. As the temperature and relative humidity increase from ambient conditions to a desired operating condition, these key parameters are reduced. The reduction factors applied for these parameters are derived from the experimental data presented in Section 3.

3. Uniaxial numerical simulations and verifications

3.1. Experimental procedure

Membrane specimens used for tensile experiments were taken from a single batch of commercially available standard dispersion cast PFSA membrane. For our comparative studies, catalyst coated membrane (CCM) samples containing the same PFSA membranes were provided by Ballard Power Systems. The membrane and catalyst layers of the CCM samples were of comparable thickness. To ensure consistency, rectangular samples were cut along the transverse direction for both membrane and CCM. Before testing, the as-received samples were kept at room conditions without any conditioning. The width of the samples was measured using an optical microscope while the thickness was measured with a digital micrometer.

A dynamic mechanical analyzer (TA Instruments Q800 DMA) equipped with an environmental chamber (TA Instruments DMA-RH Accessory) with temperature and humidity control was used for all tensile measurements. To avoid stress concentration effects at the sample edges, we used a length to width aspect ratio of 5:1 and a sample length of 10 mm. After installing the sample in the tension clamp at controlled ambient conditions, a small force was applied to keep the sample in place while the humidity and temperature were raised to the desired levels. Once the desired humidity and temperature conditions were achieved, the sample was kept in that condition for at least 30 min to allow it to equilibrate. The specimen was gradually stretched under a constant strain rate while the loading force was monitored. For the unloading experiments, the stress was gradually released until the net force applied
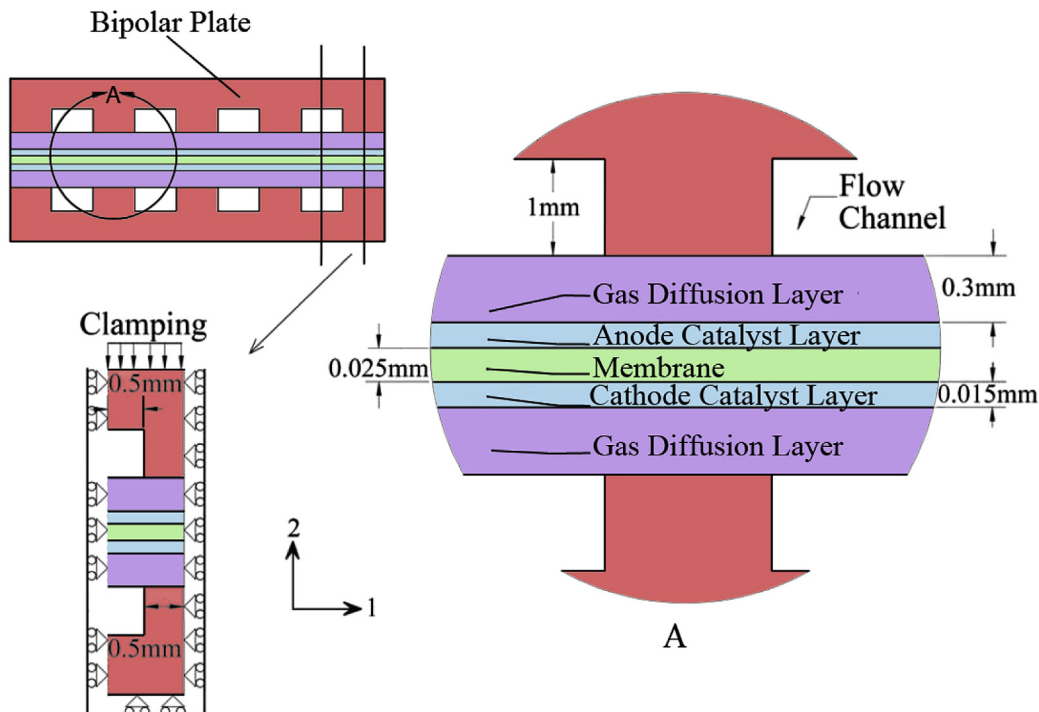

Fig. 4. Schematic of the fuel cell cross-sectional geometry and numerical domain used in the present study.

Table 2
Mechanical properties of the PFSA membrane.

μ_A	9.7×10^7 Pa
κ_A	2.1×10^8 Pa
$\dot{\gamma}^0$	71.2 s^{-1}
$\dot{\gamma}^1$	75.4 s^{-1}
ΔG	9.15×10^{-20} J
k_b	1.3806×10^{-23} J K^{-1}
s_{A1}^0	5.68×10^6 Pa
h_{A1}	4.12×10^8 Pa
s_{A1-sat}	10.52×10^6 Pa
h_{A2}	2.71×10^7 Pa
h_{A3}	3.55×10^7 Pa
s_{A3-sat}	1.25×10^7 Pa
μ_{BS}	2.57×10^7 Pa
s_{BS}^0	1.3×10^5 Pa
s_{BS-sat}	2.37×10^7 Pa
h_{BS}	4.83×10^7 Pa
μ_B	2.67×10^6 Pa

to the sample was zero. More details on the experimental approach and measured mechanical behavior of catalyst coated membranes can be found in a previous report by our group [23].

3.2. Simulated results and verifications

3.2.1. Uniaxial tension

Based on the suggested constitutive relation for the CCM, a subroutine was implemented in a finite element model using ABAQUS 6.11 and the ex-situ uniaxial tensile response of the PFSA membrane and CCM was simulated. To keep the consistency between the numerical and experimental results, the same length to width aspect ratio of 5:1 was used for simulations. Mesh independence and convergence was assured in all simulations.

In Fig. 2, comparisons between the simulated and experimental results for the PFSA membrane and CCM are provided. This set of results was obtained with a fixed strain rate of 0.0001 s^{-1}. The data shown here represent the true stress versus the true strain at four different combinations of temperature and relative humidity (RH). In the case of a pure membrane, there is generally good agreement between the numerical and experimental results for the strain under all environmental conditions with less than 20% deviation overall. The largest deviation is found at high levels of strain and high temperature. It is expected that the membrane will primarily experience low levels of strain inside a fuel cell where the present model provides a good agreement with experimental data (less than 1% overall deviation). The numerical results for higher strain rates were also compared with those reported in Ref. [23] and a similar agreement was found. Qualitatively, the obtained results for

the membrane are consistent with previous numerical results from the literature [11]. In agreement with [11], both the numerical and experimental results revealed that an increase in the relative humidity or temperature level results in decreasing the yield and tangent modulus of the membrane.

Fig. 2 also provides a comparison between the numerical and experimental results for the CCM. Similar to the case for the pure membrane, the strain rate shown here was 0.0001 s^{-1} for both simulations and experiments [23]. The CCM exhibits elastic—viscoplastic behavior consistent with that of the membrane; though the composite CCM material is softer and weaker than the membrane, as indicated by the lower yield point associated with the addition of the catalyst layers [23]. As can be seen from this figure, in all four combinations of relative humidity and temperature conditions that were applied, there is a good agreement between the simulated and experimental results for the complete range of strain considered. The maximum deviation for this data set was only 1%. Based on these results, the present constitutive model for the CCM appears to be a reliable tool for simulation of tensile stress—strain characteristics under a wide range of fuel cell relevant environmental conditions and strain rates.

3.2.2. Uniaxial unloading

In this section, the tensile unloading characteristics of the constitutive relations are examined. Experimentally, a CCM sample was gradually stretched at controlled ambient conditions and 0.0001 s^{-1} strain rate until the total true strain was approximately 50%. After equilibration, the loading force was gradually released at constant negative strain rate until the net applied force was zero. The obtained experimental results are shown in Fig. 3, and compared to the corresponding numerical simulation with the constitutive model for the CCM. As can be seen from the figure, there is a good agreement between the experimental and numerical results. During the loading phase, the deviations between the simulation and experimental results are almost negligible. On the other hand, there is a slight difference between the simulated and experimental results during the unloading process. This deviation may be due to inaccuracy in the reduction factor for the back stress mechanism. The simulated unloading results obtained at other conditions (not shown here for brevity) were also in relatively good agreement with the corresponding experimental data (less than 5% overall deviation). Hence, the present CCM model is considered to be validated for both loading and unloading mechanisms under a range of strain rates and environmental conditions relevant for fuel cell operations.

Table 3
Mechanical properties of the CCM.

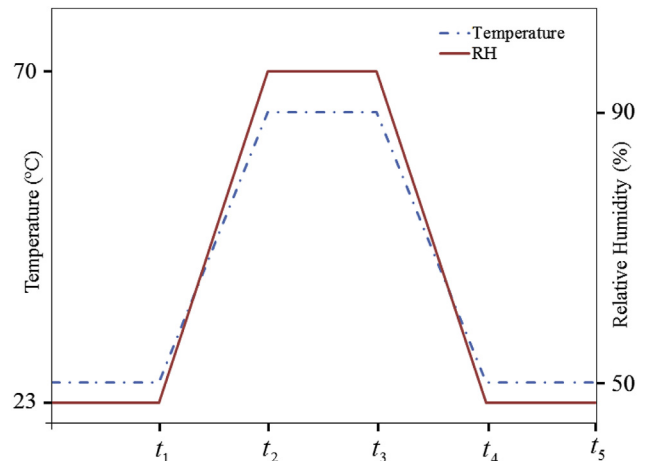|	
μ_A	6.6×10^7 Pa
κ_A	1.4×10^8 Pa
$\dot{\gamma}^0$	544.3 s^{-1}
$\dot{\gamma}^1$	1.12×10^4 s^{-1}
ΔG	9.34×10^{-20} J
k_b	1.3806×10^{-23} J K^{-1}
s_{A1}^0	5.32×10^6 Pa
h_{A1}	3.78×10^8 Pa
s_{A1-sat}	10.13×10^6 Pa
h_{A2}	2.01×10^7 Pa
h_{A3}	1.3×10^7 Pa
s_{A3-sat}	1.92×10^7 Pa
μ_{BS}	7.5×10^6 Pa
s_{BS}^0	1.3×10^6 Pa
s_{BS-sat}	6.57×10^8 Pa
h_{BS}	1.01×10^7 Pa
μ_B	2.21×10^6 Pa

Fig. 5. Schematic of the applied hygrothermal loading cycle.
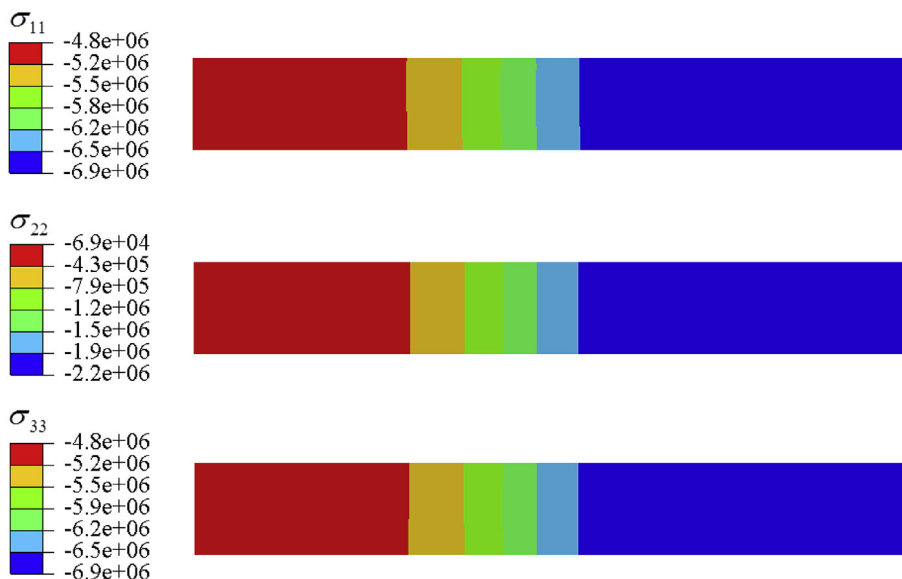
Fig. 6. Simulated stress distribution inside the membrane obtained using the membrane model at the hydrated state after fast loading (unit: Pa. Not to scale.). The right half is vertically compressed under the lands, while the left half is situated between the anode and cathode channels and supported only by the adjacent MEA components.

4. In-situ numerical simulations

The developed constitutive model for the CCM was applied to simulate the in-situ mechanical response of an MEA exposed to hygrothermal loading conditions inside a fuel cell. Due to the excessive computational cost of using a three-dimensional geometry for the cell, the symmetric properties were exploited to reduce the domain to a two-dimensional unit cell geometry. The chosen domain geometry is consistent with previous literature [11] and illustrated in Fig. 4.

In the numerical modeling, several assumptions have been made with respect to the mechanical properties of the MEA components and plates. Thermal expansion of the plates and gas diffusion layers was neglected due to the moderate operating temperatures. The plates were assumed to have a linear elastic constitutive relation with an elastic modulus of 10 MPa and a Poisson's ratio of 0.25. The gas diffusion layer material was

assumed to be orthotropic with properties adopted from Ref. [11]. Due to the symmetry conditions applied to the present domain (Fig. 4), it was assumed that the left and right hand side boundaries are constrained with respect to horizontal motion and the bottom boundary is constrained with respect to vertical motion. Two different approaches were considered for modeling the mechanical behavior of the PFSA membrane and catalyst layers. In the first approach, referred to as the *Membrane Model*, the PFSA membrane was assumed to be elastic−viscoplastic with the material constants listed in Table 2. Furthermore, the catalyst layers were assumed to be elastic−plastic, in accordance with previous literature [11]. In the second approach, referred to as the *CCM Model*, the catalyst layers and membrane are treated as a composite object with time dependent elastic−viscoplastic behavior. The material properties for this approach are summarized in Table 3. As described previously, the tensile properties of the PFSA membrane and CCM are measured in the in-plane direction. However, since the polymer
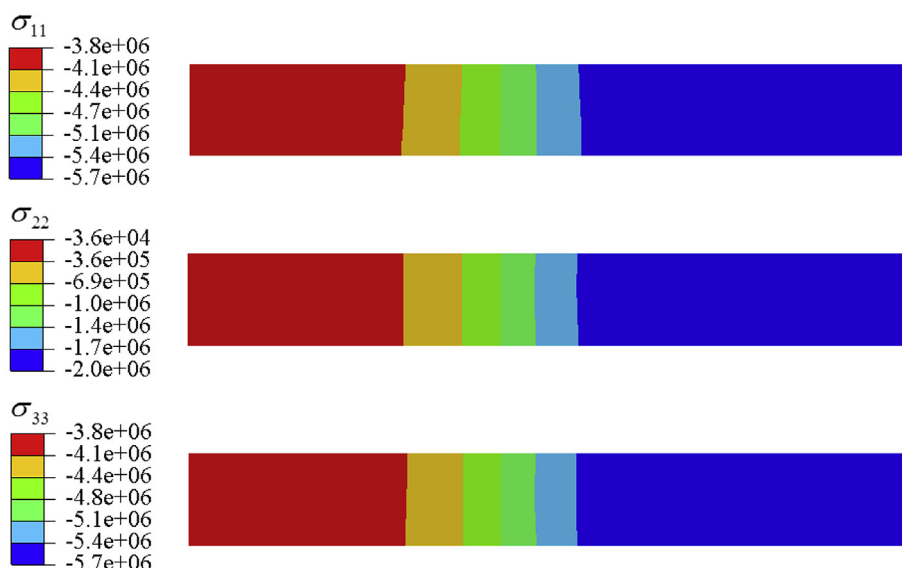

Fig. 7. Stress distribution inside the membrane obtained using the CCM model at the hydrated state after fast loading (unit: Pa. Not to scale.).
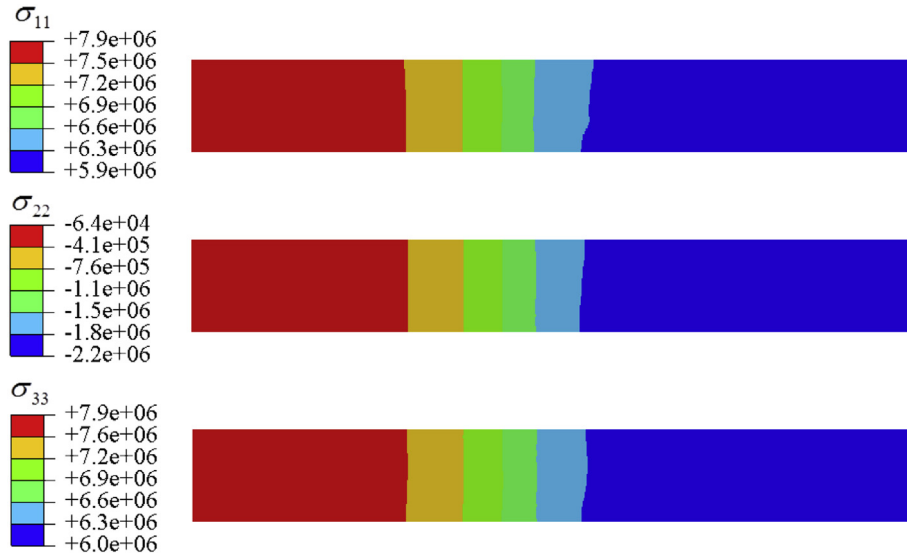
Fig. 8. Stress distribution inside the membrane obtained using the membrane model at the dried state after fast unloading (unit: Pa. Not to scale.).

morphology is generally believed to be isotropic, the same properties are assumed to be valid for the through-plane direction, in keeping with previous literature in this field [14,15]. It should be noted that in the CCM model an isotropic volume expansion due to changes in humidity and temperature is assumed. Hence, the interfacial stresses due to volume expansion between the catalyst layers and membrane are neglected. Existing studies in the literature [11,20] indicate that the overall changes in stress and strain characteristics derived from multiple, repeated hygrothermal cycles are minor. Therefore, the present study is focused on simulation of a single hygrothermal cycle. A typical hygrothermal loading condition is shown in Fig. 5. During the entire cycle, a constant cell compression pressure of 1 MPa was applied to the bipolar plates. From t_1 to t_2, the humidity and temperature were increased from an ambient condition (23 °C − 50% RH) to a standard fuel cell condition (70 °C − 90% RH) and held at this condition until t_3. From t_3 to t_4 the temperature and relative humidity were decreased from the fuel cell condition back to the ambient condition and held until t_5.

Two different loading rates were considered: a fast loading rate with a constant time step of 5 s; and a slow loading rate with a constant time step of 50 s. In the following numerical results, these two types of analyses are referred to as "Fast Loading" and "Slow Loading", respectively. During the initial steady phase of the loading curve, the only source of loading is the external pressure from the bipolar plates. Hence, all stresses are compressive and the maximum stresses occur under the land. Based on the present cell geometry, the maximum stress was found to be around 2 MPa for the σ_{22} stress component, which acts in the through-plane direction. The stresses in the other two principal directions (in-plane) were at least one order of magnitude lower. As the relative humidity and temperature are increased, the membrane tends to elongate in all three directions due to increased hydration and thermal expansion.

The numerical results were analyzed in more detail at two different time instants on the loading curve. The first point was taken after hygrothermal loading midway through the steady phase between t_2 and t_3 and referred to as the "Hydrated State". The
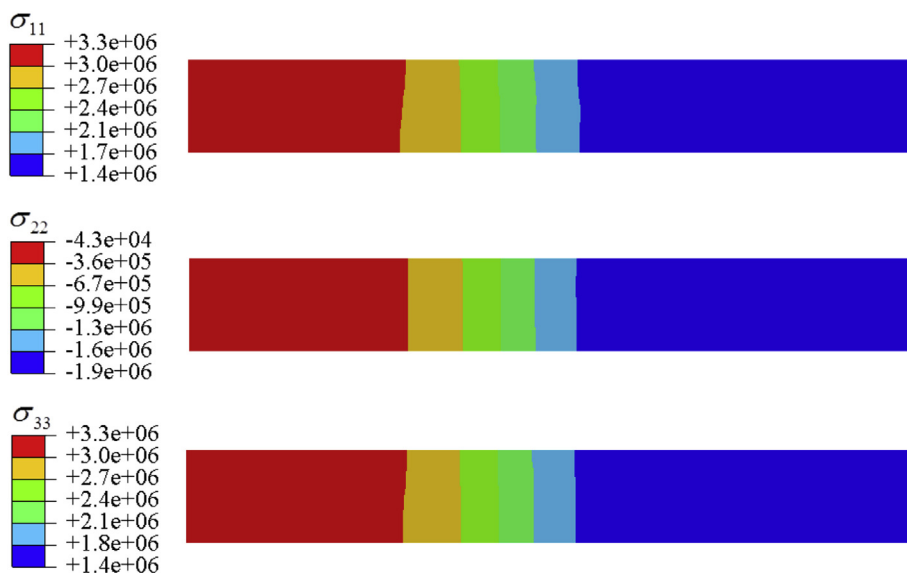

Fig. 9. Stress distribution inside the membrane obtained using the CCM model at the dried state after fast unloading (unit: Pa. Not to scale.).
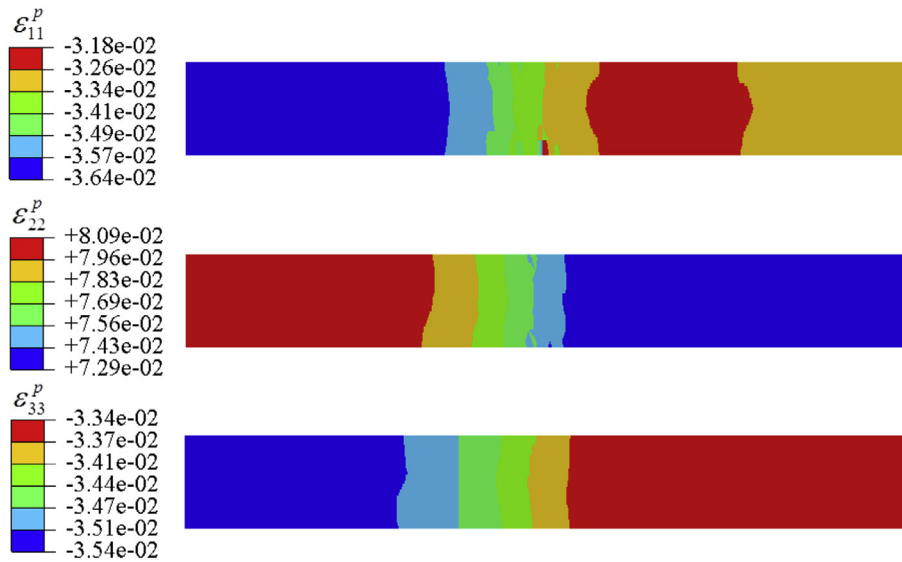
Fig. 10. Plastic strain distribution inside the membrane obtained using the membrane model at the hydrated state after fast loading.

second point was taken after the subsequent hygrothermal unloading at t_5 and referred to as the "Dried State". Fig. 6 shows the simulated stress distribution inside the membrane obtained using the membrane model at the hydrated state after fast loading. It should be noted that the side bar limits were chosen to represent the maximum and minimum stress in each specific case. The right half of the membrane is situated under the lands of the bipolar plates while the left half is located under the hydrogen and air channels. In the two in-plane directions (σ_{11}, σ_{33}), the MEA is fully constrained and experiences high stresses due to the rapid membrane hydration and expansion. In the through-plane direction (σ_{22}), the membrane is supported by predominantly elastic materials with lower modulus and is relatively free to expand. Hence, the through-plane membrane stresses are relatively low, in particular under the channel where no external compression pressure is applied. Provided that a plane strain assumption was made, the maximum and minimum stresses in the two in-plane directions are nearly identical.

The corresponding numerical results based on the CCM model at the hydrated state after fast loading are plotted in Fig. 7. This model also predicts higher compressive in-plane stresses than those in the through-plane direction. Interestingly, a comparison between the stress contour plots in Figs. 6 and 7 reveals that the membrane model over predicts the stresses in the membrane compared to the CCM model. Based on the membrane model, the in-plane stresses in the hydrated state are approximately 20% higher than for the CCM model. Similarly, the membrane model prediction for the through-plane stress is ∼10% higher under the land and up to ∼100% higher under the channel when compared to the results obtained with the CCM model. This trend is attributed to the differences in the yield point of the membrane and CCM, as measured [23]. Provided that the CCM yields at a lower stress than the membrane, the actual stress experienced in-situ is lower in the CCM than in the membrane. Based on the tensile properties, the in-plane stress levels of both objects are in the viscoplastic regime. In the through-plane direction, the membrane stress is in the elastic
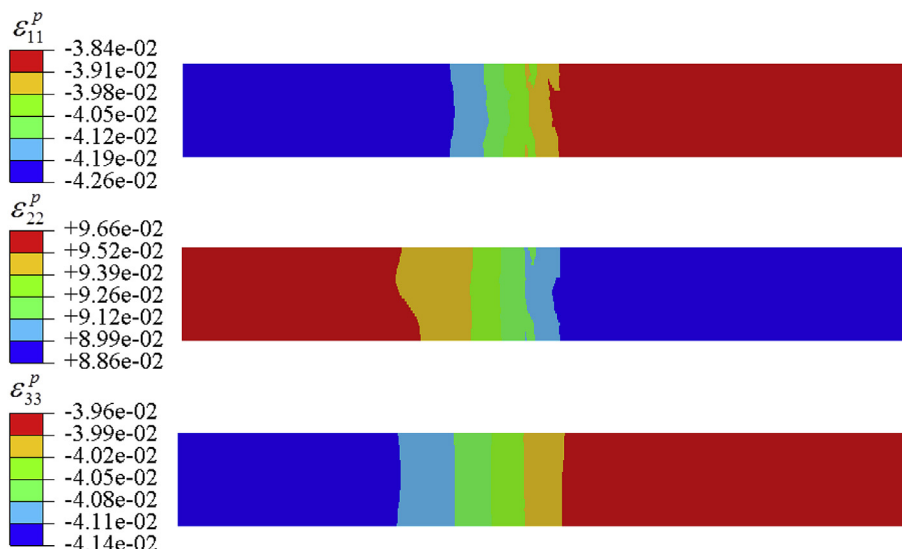

Fig. 11. Plastic strain distribution inside the membrane obtained using the CCM model at the hydrated state after fast loading.
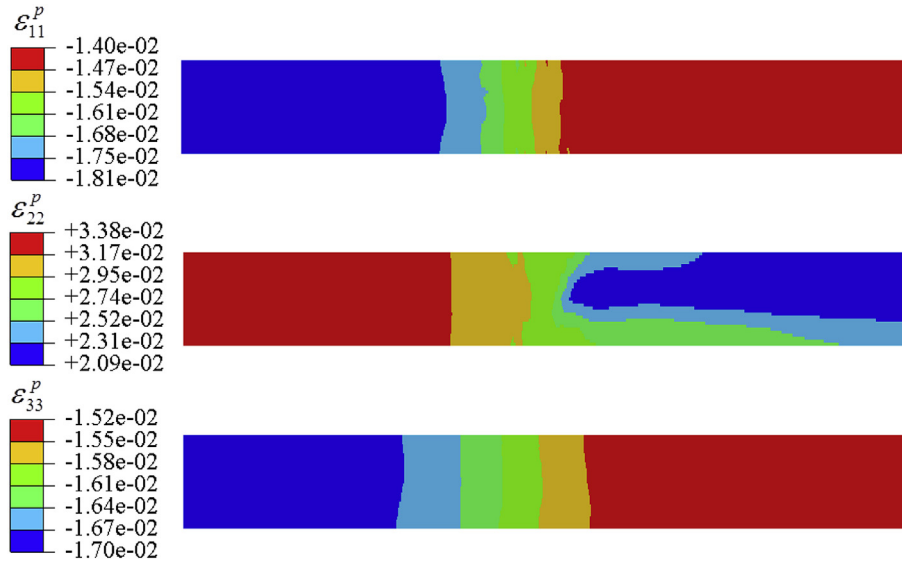
Fig. 12. Plastic strain distribution inside the membrane obtained using the membrane model at the dried state after fast unloading.

regime while the CCM stress is elastic under the channel and viscoplastic under the land.

Material fatigue due to cyclic hygrothermal and mechanical loading is a major cause of mechanical membrane degradation [6]. While high maximum stress can result in plastic deformation, a high peak-to-peak variation in stress during prolonged hygrothermal cycling may accelerate fatigue induced failures. Therefore, the stress levels after hygrothermal unloading are also of interest. Fig. 8 shows the stress distribution inside the membrane obtained using the membrane model at the dried state after fast unloading. A comparison between Figs. 6 and 8 reveals that at the dried state the in-plane stresses have changed from compressive to tensile (positive) due to membrane dehydration and contraction. In agreement with previous literature [11], the magnitude of the tensile stress at the dried state is higher than the compressive stress in the hydrated state. It is also noteworthy that the location of maximum stress has changed from under the land (hydrated state) to under the channel (dried state). Due to the dominant external compression pressure, the through-plane stresses in the dried state are still compressive.

In Fig. 9, the corresponding numerical results for the CCM model are shown. The overall trends of the CCM and membrane models are consistent: both predict in-plane tensile stresses and through-plane compressive stresses in the dried state. However, the maximum tensile stress obtained with the CCM model is ∼60% lower than for the membrane model. Additionally, when the complete CCM is considered, the stress magnitude in the dried state is found to be lower than that in the hydrated state, in contrast to the findings for the pure membrane. This indicates that the membrane model may substantially over predict the tensile stresses in the dried state. The over-prediction is less significant in the through-plane direction as a result of the dominating external compression. Based on the tensile properties, both membrane and CCM stress levels remain in the elastic regime in this state.

In the next step we investigate the effect of the cyclic loading on the strain distributions in the membrane, starting with the hydrated state after fast loading. The present study is focused on the plastic strain contribution, as opposed to the elastic, recoverable strain (found to be about 3% for comparative purposes). The plastic strain
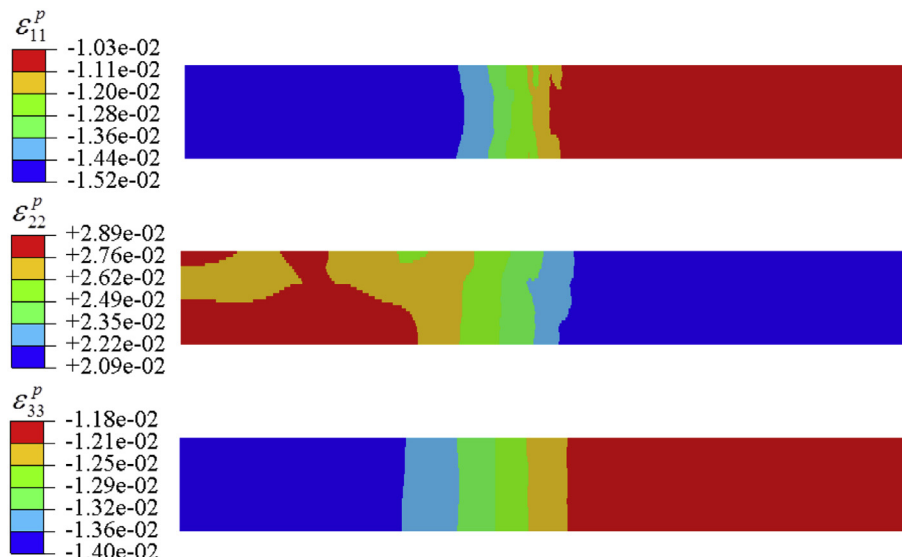

Fig. 13. Plastic strain distribution inside the membrane obtained using the CCM model at the dried state after fast unloading.
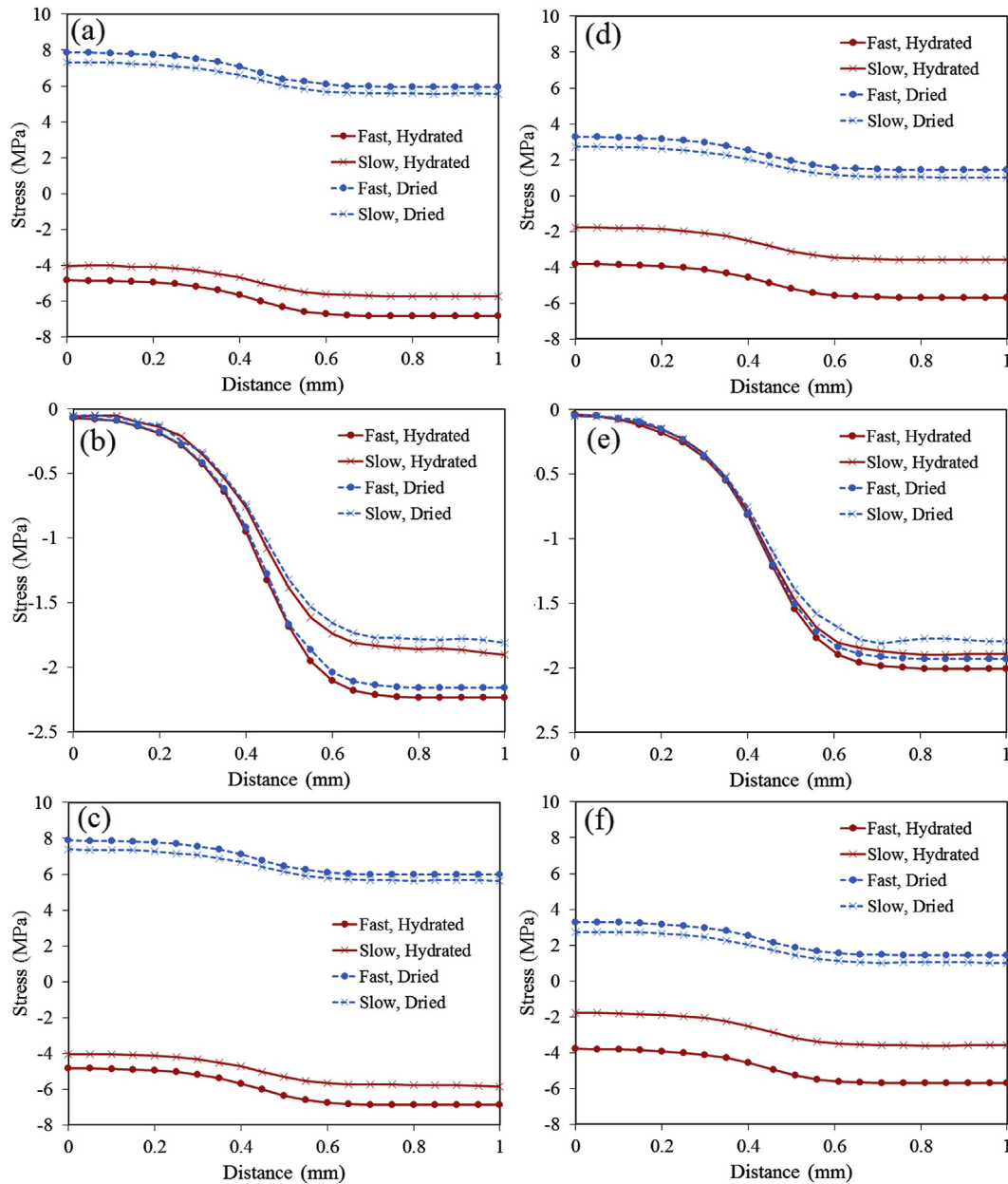
Fig. 14. Stress distribution along the centerline of the membrane obtained based on the fast and slow loading rates at the hydrated and dried states for (a) σ_{11}, (b) σ_{22} and (c) σ_{33} using the membrane model; and for (d) σ_{11}, (e) σ_{22} and (f) σ_{33} using the CCM model. The horizontal axis indicates the distance from the center of the air channel (0) to the center of the land (1).

distribution obtained using the membrane model is plotted in Fig. 10. The in-plane plastic strain in this state is found to be negative (compressive), with somewhat higher magnitude under the channel. These results are consistent with those found for the stress as the membrane/MEA is physically constrained with respect to in-plane expansion. Provided that the membrane is allowed to expand in the through-plane direction, however, significant positive (tensile) plastic strains are found in this direction as a result of the rapid hygrothermal loading. In Fig. 11, the corresponding results for the CCM model are provided. It can be seen that the CCM model predicts ∼20% higher plastic strains compared to the membrane model. This is attributed to the lower yield point of the CCM compared to the membrane, which results in more severe plastic deformation.

The results obtained with the membrane model at the dried state are depicted in Fig. 12. The plastic strain magnitude in the

dried state is significantly lower than in the previously analyzed hydrated state (Fig. 10) due to partial recovery of the plastic strain during hygrothermal unloading (drying). However, the net in-plane strain is still negative while the through-plane strain remains positive. The corresponding results for the CCM model are provided in Fig. 13. The CCM model also predicts a notable plastic strain recovery during the hygrothermal unloading. Comparing Figs. 12 and 13 reveals that at the dried state, the CCM model predicts ∼15–20% lower plastic strains than the membrane model, thus indicating a higher degree of strain recovery when the full CCM is considered.

In the next step, the effect of loading rate is investigated by comparing numerical results for the fast and slow hygrothermal cycles. Provided that the spatial stress–strain distributions are approximately one-dimensional, as shown above, the present results are reported along the centerline of the membrane. The stress
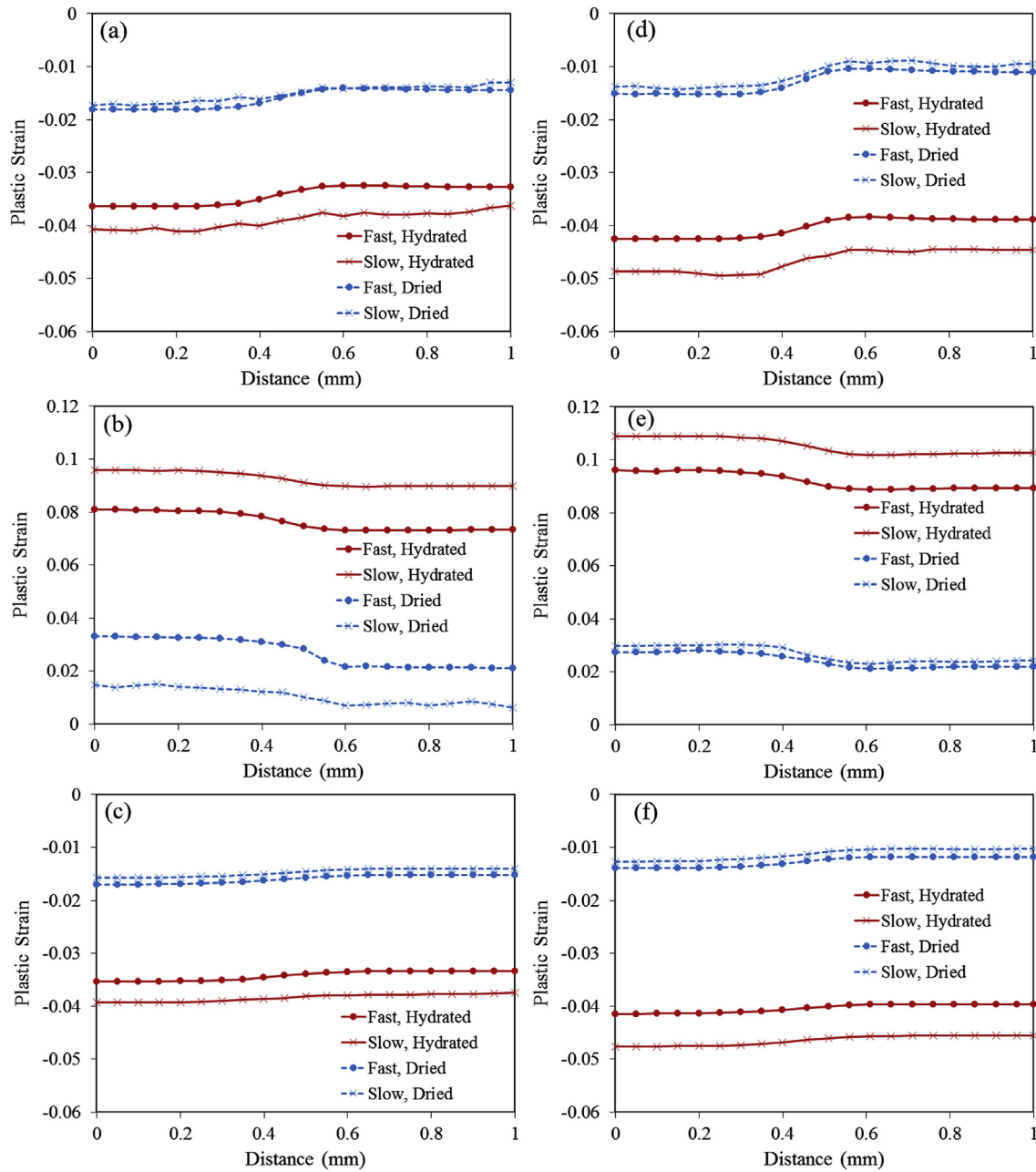
Fig. 15. Plastic strain distribution along the centerline of the membrane based on the fast and slow loading rates at the hydrated and dried states obtained using the membrane model for (a) ε_{11}^P, (b) ε_{22}^P and (c) ε_{33}^P; and using the CCM model for (d) ε_{11}^P, (e) ε_{22}^P and (f) ε_{33}^P.

results based on the membrane and CCM models at both the hydrated and dried states are provided in Fig. 14. Owing to the viscoplastic characteristics of the membrane, its response to hygrothermal loads is a function of rate [23]. The main finding in this case is that the membrane experiences lower overall stress at the slow loading rate in both the hydrated and dried states and in all three principal directions. This feature is expected to be a consequence of stress relaxation at lower loading rates.

The equivalent stress results obtained with the CCM model are also provided in Fig. 14. The overall effects of loading rate appear to be similar to those found with the membrane model; however, the reduction in stress at the slow loading rate is less significant in the through-plane direction and more significant in the in-plane direction. Due to the dominating in-plane stress, the membrane

model may again overestimate the stress at slow loading rates, and possibly more severely than at high rates.

The effect of loading rate on the plastic strain distribution inside the membrane is investigated in Fig. 15 with the membrane and CCM models. When compared to the fast loading rate, the slow loading rate results in reduced plastic strain in the dried state and increased plastic strain in the hydrated state where the highest levels of strain are found. This observation is likely a result of membrane creep, which leads to gradually increased strain with time in the hydrated state. Similar to the previously considered fast loading rate, the CCM model predicts higher plastic strain levels than the membrane model at the slow loading rate. Even through the catalyst layers are determined to reinforce the membrane which results in a stiffer and stronger object, the overall CCM

material is softer and weaker than the membrane material due to the more porous nature of the catalyst layers. Therefore, the membrane model may underestimate the plastic strain while the stress is overestimated when compared to the results obtained with the complete CCM model.

5. Conclusions

In this article, an elastic–viscoplastic constitutive model was developed and utilized to characterize the ex-situ and in-situ response of the catalyst coated membrane (CCM) under the application of mechanical and hygrothermal loading. Through validation with experimental data, the constitutive relation for the CCM was shown to be capable of predicting the nonlinear loading and unloading behavior of the CCM under a wide range of hygrothermal conditions and strain rates.

To investigate the in-situ mechanical response of the CCM during fuel cell operation, two different finite element modeling approaches were adopted: the CCM model based on the CCM constitutive relation for the PFSA membrane and the catalyst layers as a composite material, and the membrane model based on an established PFSA membrane constitutive relation with the catalyst layers treated as a separate elastic–plastic material.

In-situ numerical investigations revealed that both the CCM and membrane models predict compressive stresses at the hydrated state and tensile stresses at the dried state during a typical hygrothermal cycle. However, compared to the results obtained with the CCM model, the membrane model was found to significantly overestimate the stress in the membrane. This discovery is attributed to the weaker nature of the CCM material, which yields at a lower stress than the membrane, and therefore experiences lower overall stress when exposed to hydrothermal cycling.

Both models predicted substantial plastic strain inside the membrane, with maximum levels in the hydrated state. Notably, the plastic strain was found to be positive (tensile) in the through-plane direction and negative (compressive) in the in-plane directions due to the MEA being fully constrained in the in-plane direction. The CCM model produced higher strain than the membrane model in the hydrated state, but also allowed for more significant strain recovery during hygrothermal unloading (drying), possibly due to nonlinear unloading behavior which is subject to further research.

The in-situ response of the membrane was also found to depend on the hygrothermal loading rate. Due to the viscoplastic characteristics of the CCM and membrane materials, the stress increased with loading rate in all cases. In contrast, the plastic strain in the hydrated state decreased with increasing loading rate, which is likely a result of membrane creep and the associated time spent in the hydrated state.

Overall, the treatment of the CCM as a composite object in the in-situ simulations was found to more accurately predict the appropriate levels of stress and strain compared to the membrane model. Provided that the CCM material behaves differently than the membrane as a distinct object, it is important to consider these characteristics and to utilize a CCM based model when attempting to simulate in-situ mechanical behavior of an MEA when operated inside a fuel cell.

The findings and recommendations of the present work may also have implications for the mechanical degradation of the membrane known to occur during humidity cycling. Considering that the overall CCM material is weaker than the membrane material, and yields at a lower stress level, it is expected that microcracks may initiate in the weaker catalyst layers and propagate into the membrane during cyclic operation.

Acknowledgments

References

[1] X. Yan, M. Hou, L. Sun, H. Cheng, Y. Hong, D. Liang, Q. Shen, P. Ming, B. Yi, J. Power Sources 163 (2007) 966–970.
[2] R. Borup, J. Meyers, B. Pivovar, Y.S. Kim, R. Mukundan, N. Garland, D. Myers, M. Wilson, F. Garzon, D. Wood, P. Zelenay, K. More, K. Stroh, T. Zawodzinski, J. Boncella, J.E. McGrath, M. Inaba, K. Miyatake, M. Hori, K. Ota, Z. Ogumi, S. Miyata, A. Nishikata, Z. Siroma, Y. Uchimoto, K. Yasuda, K. Kimijima, N. Iwashita, Chem. Rev. 107 (2007) 3904–3951.
[3] Y. Tang, A.M. Karlssona, M.H. Santarea, M. Gilberta, S. Cleghornb, W.B. Johnson, Mater. Sci. Eng. A 425 (2006) 297–304.
[4] Y. Tang, A. Kusoglu, A.M. Karlsson, M.H. Santare, S. Cleghorn, W.B. Johnson, J. Power Sources 175 (2008) 817–825.
[5] A. Kusoglu, Y. Tang, M. Lugo, A.M. Karlsson, M.H. Santare, S. Cleghorn, W.B. Johnson, J. Power Sources 195 (2010) 483–492.
[6] T.T. Aindow, J. O'Neill, J. Power Sources 196 (2011) 3851–3854.
[7] S.F. Burlatsky, M. Gummalla, J. O'Neill, V.V. Atrazhev, A.N. Varyukhin, D.V. Dmitriev, N.S. Erikhman, J. Power Sources 215 (2012) 135–144.
[8] A. Kusoglu, Y. Tang, M.H. Santare, A.M. Karlsson, S. Cleghorn, W.B. Johnson, J. Fuel Cell Sci. Technol. 6 (2009) (Article#011012).
[9] W. Yoon, X. Huang, J. Power Sources 196 (2011) 3933–3941.
[10] Z. Lu, C. Kim, A.M. Karlsson, J.C. Cross. III, M.H. Santare, 196 (2011) 4646–4654.
[11] N.S. Khattra, A.M. Karlsson, M.H. Santare, P. Walsh, F.C. Busby, J. Power Sources 214 (2012) 365–376.
[12] R. Solasi, Y. Zou, X. Huang, K. Reifsnider, D. Condit, J. Power Sources 167 (2007) 366–377.
[13] D. Bograchev, M. Gueguen, J.C. Grandidier, S. Martemiannov, Int. J. Hydrogen Energy 33 (2008) 5703–5717.
[14] A. Kusoglu, A.M. Karlsson, M.H. Santare, S. Cleghorn, W.B. Johnson, J. Power Sources 161 (2006) 987–996.
[15] A. Kusoglu, A.M. Karlsson, M.H. Santare, S. Cleghorn, W.B. Johnson, J. Power Sources 170 (2007) 345–358.
[16] R. Solasi, X. Huang, K. Reifsnider, Mech. Mater. 42 (2010) 678–685.
[17] R. Solasi, Y. Zou, X. Huang, K. Reifsnider, Mech. Time-Depend. Mater. 12 (2008) 15–30.
[18] M.N. Silberstein, M.C. Boyce, J. Power Sources 195 (2010) 5692–5706.
[19] M.N. Silberstein, P.V. Pillai, M.C. Boyce, Polymer 52 (2011) 529–539.
[20] M.N. Silberstein, M.C. Boyce, J. Power Sources 196 (2011) 3452–3460.
[21] K.K. Poornesh, Y.J. Sohn, G.G. Park, T.H. Yang, Int. J. Hydrogen Energy 37 (2012) 15339–15349.
[22] W. Yoon, X. Huang, J. Electrochem. Soc. 157 (2010) B680–B690.
[23] M.A. Goulet, R.M.H. Khorasany, C.D. Torres, E. Kjeang, M. Lauritzen, G. Wang, N. Rajapakse, J. Power Sources 234 (2013) 38–47.
[24] J.S. Bergstrom, M.C. Boyce, J. Mech. Phys. Solids 46 (1998) 931–954.
[25] J.S. Bergstrom, M.C. Boyce, Mech. Mater. 32 (2000) 627–644.
[26] E.M. Arruda, M.C. Boyce, R. Jayachandran, Mech. Mater. 19 (1995) 193–212.